SEISMIC DISCONTINUITIES IN THE MANTLE BENEATH THE WESTERN PACIFIC: EVIDENCE FROM SCS REVERBERATIONS

A Senior Scholars Thesis

by

BRIAN C. BAGLEY

Submitted to the Office of Undergraduate Research
Texas A&M University
in partial fulfillment of the requirements for the designation as

UNDERGRADUATE RESEARCH SCHOLAR

April 2006

Major: Geophysics

SEISMIC DISCONTINUITIES IN THE MANTLE BENEATH THE WESTERN PACIFIC: EVIDENCE FROM SCS REVERBERATIONS

A Senior Scholars Thesis

by

BRIAN C. BAGLEY

Submitted to the Office of Undergraduate Research
Texas A&M University
in partial fulfillment of the requirements for designation as

UNDERGRADUATE RESEARCH SCHOLAR

Approved by:

Research Advisor:	David Sparks
Associate Dean for Undergraduate Research:	Robert C. Webb

April 2006

Major: Geophysics

ABSTRACT

Seismic Discontinuities in the Mantle Beneath the Western Pacific: Evidence from ScS Reverberations (April 2006)

Brian C. Bagley
Department of Geology and Geophysics
Texas A&M University

Research Advisors: Dr. David Sparks
Department of Geology and Geophysics

Earthquakes generate seismic waves that travel through the Earth and can be reflected by changes in density and/or seismic velocity that may relate to changes in the phase or chemical composition of the mantle. To study these discontinuities we use the ScS reverberative interval of seismic records. This is accomplished by inverting zeroth order waves for whole mantle properties that are used to create a profile of reflectivity vs. depth through the mantle. This profile includes the expected transition zone discontinuities. We then create a second profile through a process of iterative forward modeling to locate the depth of additional mantle discontinuities. We have selected three source-receiver paths in the western Pacific as our research area because of its high seismic activity, and the widespread coverage of seismometers. We found the expected transition zone discontinuities at 410 km and 660 km in all three paths. We found discontinuities at 83 and 288 km in path A, which samples the oceanic crust between the Marianas trench and Hawaii. In path B, which samples an area between the Izu-Bonin trench and Hawaii, we found discontinuities at 77, 321, and 2645 km. Path C, which

samples the Sea of Japan and includes the subducted Pacific plate contains discontinuities at 337, 558, 850, and 2782 km. Many of these discontinuities have been detected in previous studies using different methods [e.g., *Zang et al.,* 2003; *Revenaugh and Jordan,* 1991]. We believe the discontinuities near 300 km in paths A and B signal the presence of stishovite in eclogitic mid-upper mantle. The negative reflectivity of the feature at 337 km in path C is interpreted as evidence of a partially molten zone above the 410-km discontinuity, as has been indicated in previous studies [e.g., *Revenaugh and Sipkin*, 1994].

ACKNOWLEDGMENTS

This research was funded through a Research Experience for Undergraduates (REU) grant provided by the National Science Foundation (NSF). Centroid-Moment Tensor solutions were provided by Harvard University. All research was completed at the University of Minnesota in the summer of 2005 as part of a summer internship. I worked with Jennifer Fletcher, an intern from the University of Washington, and Justin Revenaugh, professor of Geophysics at the University of Minnesota, coordinated our efforts. Anna Courtier provided valuable training regarding the modeling programs used in our project.

TABLE OF CONTENTS

Page

LIST OF FIGURES

LIST OF TABLES

1. INTRODUCTION

The Earth's mantle is most of the planet by volume and by mass. It is complex, bookended by major thermal boundary layers at the top and bottom, and punctuated by a number of radial discontinuities, many of which are not well understood. Each represents a rapid change in velocity and/or density marking an abrupt change in crystalline phase, composition, state, or a combination of these things. We study these discontinuities to gain insight into the composition, dynamics, and state of the mantle. For this study we selected one path sampling the Izu-Bonin subduction complex, and two paths connecting earthquakes in Japan and Marianas with seismometers in Hawaii. We use the ScS reverberative interval and migration-like imaging algorithms adapted from multi-channel controlled source seismic exploration. The reverberative interval of SH-polarized seismograms is ideal for this task due to the multiplicity of arrivals sampling mantle discontinuities and the absence of high-amplitude phases, which might obscure them.

Three of the mantle's largest discontinuities are found in the transition zone, marking successive phase transitions in the olivine component of mantle silicates. Because mineralogical phase changes depend upon temperature and pressure through the Clapeyron slope, the depth to a discontinuity will vary with temperature and thus with location in the thermally heterogeneous mantle. However, we must also consider the effects of composition, which can alter the Clapeyron slope and the magnitude of phase transitions. The existence of partial melt and/or anisotropy can also lead to localized

---

This thesis follows the style and format of the Journal of Geophysical Research.

discontinuities. Far from a nuisance, the abundance of ways in which discontinuities can arise in the mantle offers numerous "windows" into mantle dynamics.

A subducting slab interacts with phase transitions in several different ways. In some regions the subducted slab will pass through discontinuities relatively unimpeded [*Revenaugh and Jordan*, 1991; and references therein], while in other cases, notably at the 660-km discontinuity, the slab will deflect and follow the top of the phase transition until it either reassimilates into the mantle or flushes through. Cold temperatures in the slab result in local elevation of the exothermic 410-km discontinuity (olivine to wadsleyite), although there is evidence of kinetic inhibition of the transition in the interior of very old, rapidly subducted slabs. The endothermic 660-km transition is depressed by the cold slab and impedes vertical convective flow [*Revenaugh and Jordan*, 1991; and references therein].

Evidence of melt above the 410-km discontinuity has been found in previous studies of this kind [*Revenaugh and Sipkin*, 1994]. However, seismological studies alone will not provide answers concerning the origin of the melt, or why the melt ponds. By mapping and characterizing the occurrence of melt in the mantle, we hope to provide the crucial constraints necessary to answer these questions. What follows will be a description of the methods we employed to locate melt and discontinuities, and a discussion of what they may possibly indicate.

2. METHODS

2.1 Data Collection

We used the ScS reverberative interval (Figure 1) that occurs after the direct Love wave and before the arrival of the first SSS or SSSdiff wave from the major arc. This interval is useful because it is dominated by high amplitude multiple ScS and sScS phases (Figure 2). An ScS_n wave is one that begins its path in a downward direction and is reflected from the core mantle boundary (CMB) and subsequently from the free surface (FS); the "n" subscript denotes the number of times it has been reflected between the CMB and the FS. The "s" in $sScS_n$ indicates that the wave is a depth phase.

Data was collected from three separate networks: Incorporated Research Institutions for Seismology (IRIS), F-net Broadband Seismograph Network, and Ocean Hemisphere Project Data Management Center (OHP DMC). Potential events were identified based on magnitude (greater than 5.7), depth (greater than 100 km), and location (receivers within 60 degrees of the event). An earthquake with a magnitude less than 5.7 does not typically generate enough energy to produce the ScS reverberations required for this method. Seismograms from earthquakes shallower than 100 km contain high amplitude surface waves early in the interval and overlapping ScS and sScS waves later in the interval, which obscure the reverberations. The ScS reverberative interval gets shorter as the epicentral distance gets longer, which also makes it difficult to isolate the waves we are interested in.

The criteria above limited the number and orientation of the paths we were able to study. Potential paths are determined by plotting the ScS surface bounce points on a

mercator map and finding regions that contain bounce points from multiple events. After selecting data that met our criteria, each seismogram was examined to determine if there were any other problems that would exclude it from the final data set. Many of the seismograms are recorded by island station seismometers, and in many cases, contain too much background noise (due to ocean waves) to be included the study. Equipment malfunctions also produce seismograms that are incomplete and considered unusable.

Because our method relies on path averaging we must be careful to include enough data. That is, relying on only a few seismograms might produce erroneous results. Each path in this study contains at least fifteen seismograms from multiple events. The three paths that characterize our final data set are shown in Figures 3 and 4. One path samples the mantle beneath the subduction complex in the Sea of Japan (path C), and two paths sample the older oceanic crust from the Izu-Bonin (path B) and Marianas (path A) trenches to Hawaii. Tables 1, 2, and 3 provide a complete list of the source receiver pairs used; the location, depth, and magnitude for each event is also listed. The names and locations of the receivers can be found in Table 4. The next step is to process the data so that it can be used to obtain the parameters necessary to create a model.

2.2. Data Processing

Because we are interested only in the S wave portion of the record the data was passband filtered, rotated, and deconvolved to obtain the SH polarized portion of the

wave. SH polarized waves do not contain mode conversions or waves that have passed through the core. These waves are also classified by order, i.e., the number of times the wave has been reflected by a mantle discontinuity (Figure 2). A zeroth order wave has not been reflected by a mantle discontinuity, only by the free surface (FS) and the core mantle boundary (CMB). Both of these are considered to be perfect reflectors, therefore, zeroth order waves maintain a high signal to noise ratio (SNR) as the waves are reflected multiple times between the CMB and FS. In addition, zeroth order waves can be inverted to determining whole mantle travel time (τ_{scs}) and average attenuation (Q_{scs}). First order waves have been reflected once inside the mantle (by a discontinuity), and higher order waves include those waves that have been reflected inside the mantle more than once. First and higher order waves are used to forward model the reflection profiles we create with zeroth order waves. Using waveforms that contain multiple reverberations also helps to compensate for the effects of attenuation and geometric spreading.

The reflection coefficient measures the impedance contrast between the two layers at the discontinuity. Impedance at normal incidence is defined as $I = \rho v$, where ρ is density and v is velocity. The reflection coefficient varies between -1 and 1, with 0 being the homogenous case where the wave is not reflected or refracted. A positive $R(z)$ indicates a velocity increase corresponding to a impedance increase with depth, and a negative $R(z)$ indicates a velocity decrease corresponding to a impedance decrease with depth.

2.3 Determining Crust and Mantle Properties

The crust is assumed to be a single homogeneous layer with constant thickness. Thickness of the crust is defined as the distance from the FS to the Mohorovicic layer (Zm), with a reflection coefficient of (R(Zm)). This is a simplification; however, a one-layer crust is a reasonable approximation for our model. A grid-searching algorithm is used to vary crustal parameters (R(Zm), Zm) and Q_{scs} until the best match is found, which is determined by variance reduction. This produces an average crustal thickness for each seismogram, which are subsequently combined to obtain an overall path average. Path averaging also compensates for the thicker continental crust that may be located at some of the source or receiver locations. The limits for the grid search are set for a maximum thickness of 35 km and a minimum thickness of 5 km. The values we used for crustal thickness and attenuation can be found in Table 5. In previous studies using ScS reverberations [e.g., Revenaugh and Jordan, 1989], the crustal values determined by the grid search method have been shown to match the results of studies using different methods.

To obtain the mantle information we need for the model we must invert first and higher order waves in the following manner

$$d^{scat} = \sum_{i=1}^{N} R(Z_i)g(Z_i) + n \qquad (1)$$

where d^{scat} is the sum of first and higher order reverberations that have been reflected by at least one internal mantle discontinuity, $R(Z_i)$ is the unknown reflection coefficient at

depth Z_i, $g(Z_i)$ is the synthetic seismogram for a single reflector at depth Z_i with unit reflection coefficient, and n is noise.

The mantle from the base of the crust to 10 km above the CMB is divided into 5 km thick layers, with each layer representing a discontinuity having an unknown reflection coefficient. The synthetic seismogram that would be generated by a discontinuity with a unit reflection coefficient ($g(Z_i)$) is calculated for each layer and stored in a matrix. The information from our actual seismograms (d^{scat}) is also entered in the matrix, with zeros for the depths where there are no reflections. This matrix can now be inverted to find the reflection coefficients at each depth where there is a discontinuity present. For a detailed explanation of this process the reader should refer to the four papers by Revenaugh and Jordan [1989—1991], in which a detailed explanation of this inversion process, along with the methods used for defining the crustal structure can be found.

The inversion results in a reflectivity profile (Figures 5 and 6), which shows how reflectivity changes with depth in the mantle. The gray band that is displayed with the data represents noise; values of reflectivity that exceed the gray band indicate a true reflector, with a confidence level of 95%.

After processing these data, and discarding the seismograms with excessive noise or otherwise bad data, we were left with the following: 22 seismograms from 21 events in path A, 15 seismograms from 13 events in path B, and 34 seismograms from 8 events in path C. Details regarding the source-receiver pairs is provided in Tables 1, 2, and 3.

2.4 Synthetic Data and the Model

For the mantle portion of the model, we used the PREM model [*Dziewonski and Anderson*, 1981] as a starting point. Initially, we assume that the Earth has a simple mantle structure that contains only two discontinuities, one at 410 km and one at 660 km. Synthetic seismograms are created using a model that contains this mantle structure and the crustal structure previously described. Adding discontinuities to the mantle model allows us to change the synthetic profile until it matches the data profile. We assume that a simple mantle with few discontinuities is preferable to a complicated mantle with many discontinuities, so we add as few discontinuities as possible to obtain a matching profile. We assume an initial depth to the discontinuity being modeled, and compare the two profiles using variance reduction to determine if they match. Our program uses an iterative forward modeling process, adjusting the depth automatically based on the results of the previous iteration. Due to the complex manner in which seismic waves interact with discontinuities, a perfect match is not possible. The goal is to obtain a model that closely resembles the data.

One of the artifacts produced by this method is the apparent symmetry around the midpoint of the reflectivity profile. This symmetry is created during the forward modeling process, and is due to the fact that each first order reverberation has two possible ray paths. That is, a topside reflection from an upper discontinuity has the same travel time as a bottom side reflection from a lower discontinuity, or vice versa. In addition, the lower half of the profile is slightly elongated since velocity increases with

depth in the mantle. Because we know that many of the discontinuities that occur in the mantle are located in the transition zone due to mineralogical phase changes, we can safely model most discontinuities in the upper mantle. The exception would be discontinuities that occur near the D" region above the CMB.

Side lobes are also produced during the modeling process. For each real peak in the data there are two corresponding peaks of opposite polarity, and smaller amplitude. The process of cross-correlation creates these side lobes. They are not always symmetric because closely spaced signals produce side lobes that interfere with one another.

3. RESULTS

Path A samples the oceanic crust between the Marianas Trench and Hawaii (Figure 5 and Table 1). In addition to the expected discontinuities found at 410 km and 660 km, there is an impedance decrease at 83 km and an impedance increase at 288 km. These two features are named G, for the Gutenberg discontinuity, and X, following Revenaugh and Jordan [1991], respectively. The one prominent feature near the base of the mantle is interpreted as the lower-mantle artifact resulting from G.

Path B samples an area between the Izu-Bonin trench and Hawaii (Figure 5 and Table 2) and contains features very similar to path A; including the 410-km, 660-km, and G. The X discontinuity is less prominent than in Path A, but a positive reflector is found at about 320 km, slightly deeper than in A. The signal for the X discontinuity in path B barely exceeds the noise level, but we chose to model it based on what we found in path A. Path B contains fewer seismograms than path A or C, which could account for the lower amplitude signal and lower SNR (wider gray band). The appearance of the X discontinuity in both paths suggests its widespread occurrence.

There is also a small impedance increase at 2645 km, which we interpret to be D''. This feature could also be modeled as an impedance decrease in the upper mantle. However, when modeled in the upper mantle, it substantially alters the appearance of the G and X discontinuities, and would require additional discontinuities to be added to create a model that matches the data profile. Given it's location near the CMB and the

desirability of the fewest number of necessary discontinuities, we interpret this as a lower mantle feature.

The subduction dominated region, Path C (Figure 6 and Table 4), produced very interesting results. In addition to the impedance increases we expected to find at 410 km and 660 km, we also found small impedance increases at 558 km and 850 km, and impedance decreases at depths of 337 km and 2782 km. Once again, we chose to model the discontinuity at 2782 km in the lower mantle because of the problems created when trying to model it in the upper mantle. The discontinuity modeled at 337 km is certainly questionable and could be interpreted as a side lobe due to the 410-km discontinuity. There is not much confidence in this feature but nonetheless it has been included. On the other hand, the feature at 850 km has been found in other studies of the Izu-Bonin region [e.g., *Zang et al.*, 2003; *Vinnik et al.,* 1998] using different methods. The feature at 558 km is believed to be a deep 520 km discontinuity, which has also been found in other studies [e.g., *Zang et al.,* 2003; *Revenaugh and Jordan,* 1991]. Notably missing from our results are the elevated 410-km discontinuity and depressed 660-km discontinuity due to the subducting slab. The effect of the subducting slab on these discontinuities is well documented in other studies [e.g., *Zang et al.,* 2003; *Revenaugh and Jordan,* 1991].

4. DISCUSSION

The 410-km and 610-km discontinuities are present in all of our paths and are well documented. Likewise, the 520-km, D'', and the Gutenberg discontinuities are also well known discontinuities that warrant no further discussion here. The remaining discontinuities found in this study are subject to some interpretation. However, we can place some constraints on their appearance by using our geologic knowledge of the region.

We interpret the X discontinuity as the phase transition from coesite to stishovite, two high-pressure polymorphs of SiO_2, which occur at pressures above 10 GPa (depths of about 300 km). A silica-rich phase would not be stable in normal peridotite mantle. Therefore, stishovite at these depths is interpreted to indicate the presence of subducted ancient oceanic crust [*Williams and Revenaugh*, 2005].

The deeper reflection at 850 km corresponds with discontinuities found in other studies of the mantle beneath the subducting Pacific plate [e.g., *Zang et al*., 2003; *Vinnik et al.,* 1998]. Both this feature and the X discontinuity indicate the presence of subducted slab material in the mantle of the western Pacific, east of the present day subduction zones. If these features are related to paleosubduction of the Pacific plate, they imply westward drift of the subduction zone or large-scale folding of the slab in the lower mantle.

The impedance decrease found in the Path C (Figure 6) is intriguing because it indicates the presence of a low-velocity layer at great depth. A liquid phase is an

obvious cause of reduced seismic velocity, and partially molten regions have been previously detected in this region of the western Pacific [*Revenaugh and Sipkin*, 1994]. The presence of magma at these depths would be unusual, and is interpreted as "melt ponding"—melt that has sunk to this depth and collected above the olivine-to-wadsleyite transition (the 410-km discontinuity). Because of their higher compressibility, basic to ultrabasic melts become denser than the surrounding mantle at pressures above 6 Gpa [*Revenaugh and Sipkin*, 1994; and references therein; *Sakamaki, et al.*, 2006], so melt would sink until it reached a neutral buoyancy depth. The presence of melt above the 410-km discontinuity is still a highly debated topic. The main reason for this is because there is no definitive explanation for the process that would cause melting under those conditions.

It is well known that the presence of water allows rocks to melt at lower temperatures. It has been suggested that the water content of the upper mantle is ~ 0.1 to 0.2 wt% [*Huang, et al.*, 2005]. At high pressure water is more compressible than the melt containing it; therefore, it would not lower the density of the melt as one might expect, and the melts would still be negatively buoyant [*Matsukage, et al.*, 2005].

To solve these unanswered questions, it will be necessary to continue to map and characterize as much of the mantle as possible. By continuing to improve our methods we hope to obtain better estimates of the depth and size of mantle discontinuities; which are the characteristics our methods are well suited to resolve. Additional earthquakes that fit our criteria will continue to occur, allowing us to collect more data, which will

improve the accuracy of our models. These models can be used as the initial models for tomographic studies, which provide us with a different perspective of the Earth's mantle.

REFERENCES

Dziewonski, A. M., and D. L. Anderson (1981), Preliminary reference Earth model, *Physics of the Earth and Planetary Interiors*, *25*, 297-356.

Huang, X., et al. (2005), Water content in the transition zone from electrical conductivity of wadsleyite and ringwoodite, *Nature*, *434*, 746-749.

Matsukage, K. N., et al. (2005), Density of hydrous silicate melt at the conditions of Earth's deep upper mantle, *Nature*, *438*, 488490.

Revenaugh, J., and T. H. Jordan (1989), A study of Mantle Layering Beneath the Western Pacific, *J. Geophys. Res.*, *94*, 5787-5813.

Revenaugh, J., and T. H. Jordan (1991a), Mantle Layering From ScS Reverberations 1. Waveform Inversion of Zeroth-Order Reverberations, *J. Geophys. Res.*, *96*, 19,749-719,762.

Revenaugh, J., and T. H. Jordan (1991b), Mantle Layering From ScS Reverberations 2. The Transition Zone, *J. Geophys. Res.*, *96*, 19,763-719,780.

Revenaugh, J., and T. H. Jordan (1991c), Mantle Layering From ScS Reverberations 3. The Upper Mantle, *J. Geophys. Res.*, *96*, 19,781-719,810.

Revenaugh, J., and S. A. Sipkin (1994), Seismic evidence for silicate melt atop the 410-km mantle discontinuity, *Nature*, *369*, 474-476.

Sakamaki, T., et al. (2006), Stability of hydrous melt at the base of the Earth's upper mantle, *Nature*, *439*, 192-194.

Vinnik, L., et al. (1998), Broadband converted phases from midmantle discontinuities, *Earth Planets Space*, *50*, 987-997.

Williams, Q., and J. Revenaugh (2005), Ancient subduction, mantle eclogite, and the 300 km seismic discontinuity, *Geology*, *33*, 1-4.

Zang, S., et al. (2003), Mantle discontinuities beneath Izu-Bonin and the implications, *Science in China. Series D, Earth Sciences*, *46*, 1201-1211.

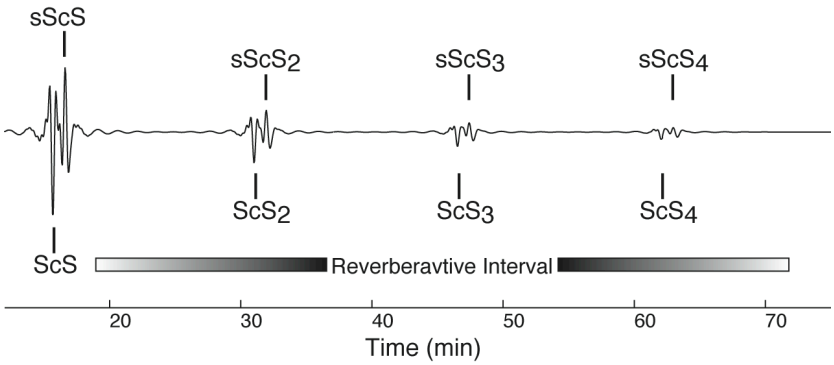

Figure 1. A synthetic SH-polarized seismogram showing zeroth-order multiple ScS and sScS phases. The time interval shown is 12 to 75 minutes after the earthquake origin. The Love wave and SSS wave used to define the reverberative interval are not shown.

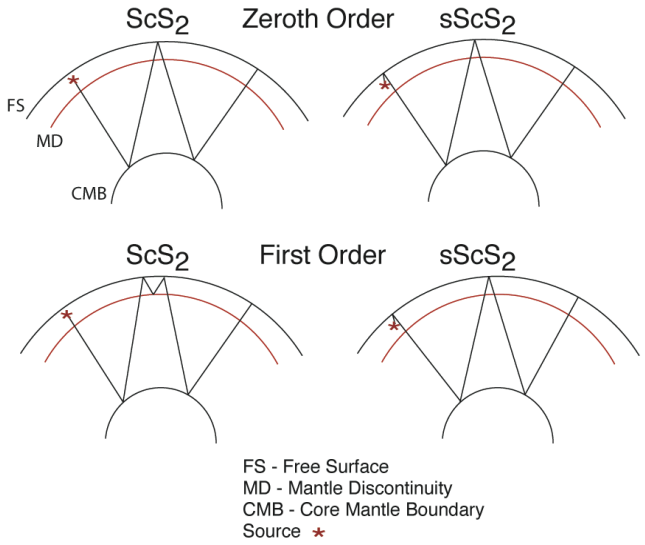

Figure 2. Diagram showing ScS reverberations between the free surface (FS), core mantle boundary (CMB), and a mantle discontinuity (MD). (Top) Zeroth-order reverberations of ScS_2 and $sScS_2$. Zeroth-order refers to the fact that it has not been reflected by any mantle discontinuities. The "2" indicates that this wave has been reflected by the core-mantle boundary two times. The "s" indicates that this wave is a depth phase. (Bottom) First-order reverberations of ScS_2 and $sScS_2$. First order indicates that this wave has been reflected once from a mantle discontinuity.

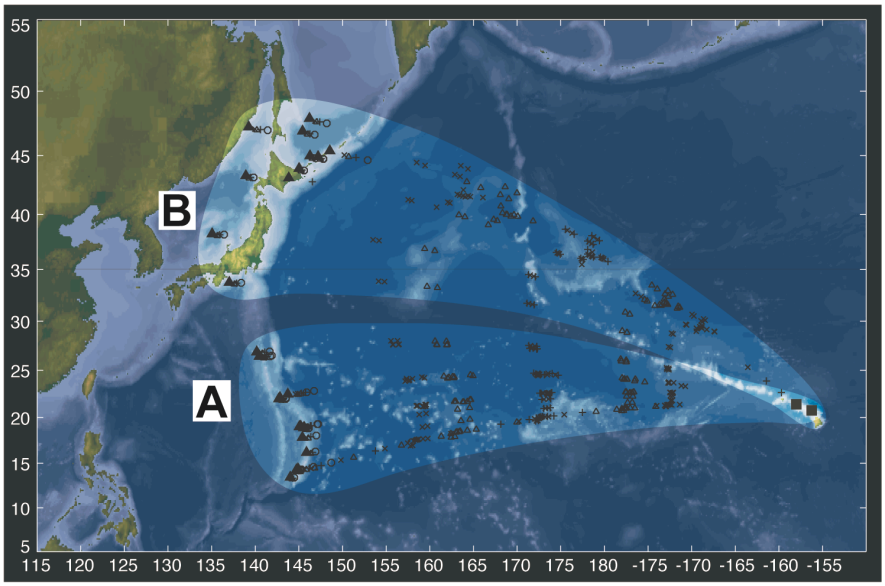

Figure 3. Mercator map of path A (Marianas to Hawaii) and path B (Japan to Hawaii), showing earthquake events (triangles) and location of seismometers (squares). The pluses, crosses, and diamonds represent the bounce points for the ScS2, ScS3, and ScS4 phases respectively.

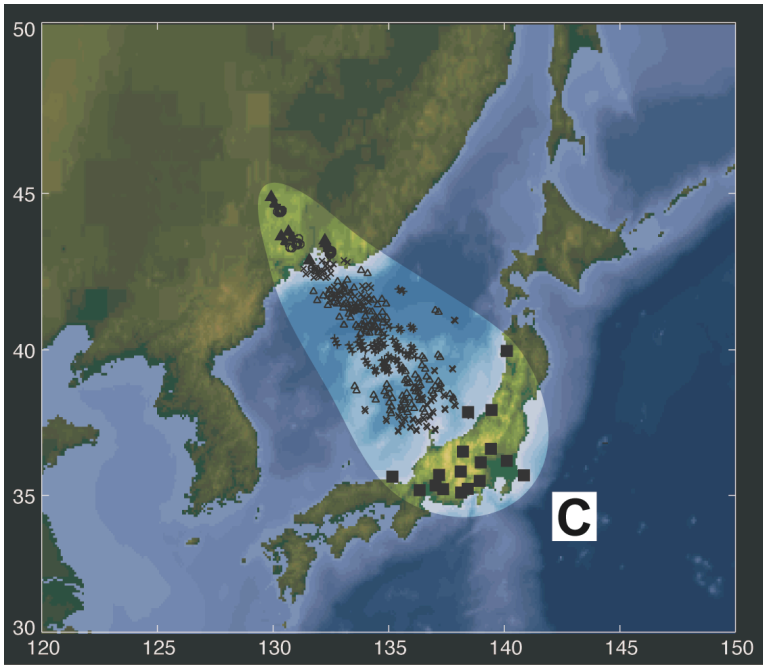

Figure 4. Mercator map of path C (Sea of Japan to Honshu) showing earthquake events (triangles) and location of seismometers (squares). The pluses, crosses, and diamonds represent the bounce points for the ScS2, ScS3, and ScS4 phases respectively.

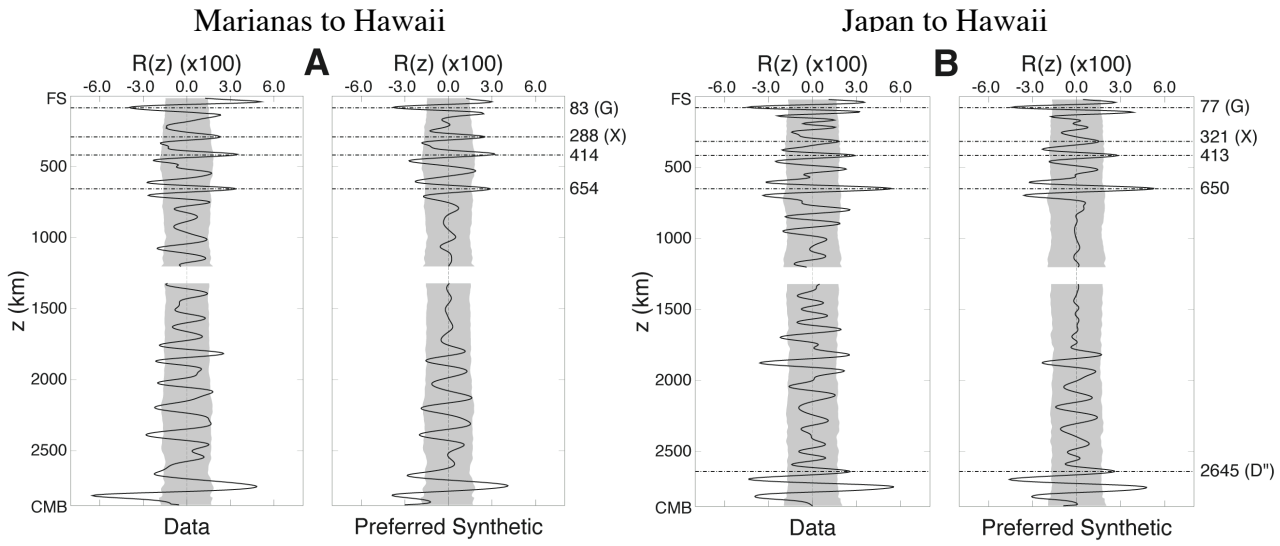

Figure 5. Comparison of data with synthetically produced data (preferred synthetic) for Paths A and B. The horizontal axis (R(z)) is reflectivity and the vertical axis (z) is depth. The gray area represents noise, signals that exceed this threshold are considered to be reliable (with a confidence level of 95%). The stack for Path A uses 22 seismograms from 21 events. The stack for path B uses 15 seismograms from 13 events.

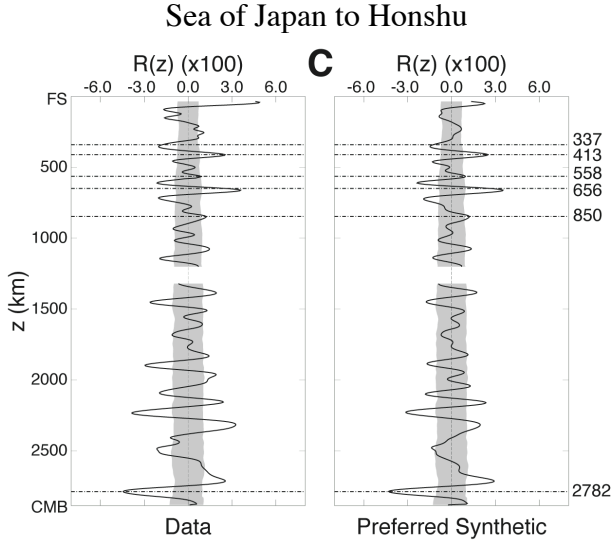

Figure 6. Comparison of data with synthetically produced data (preferred synthetic) for Paths C. The horizontal axis (R(z)) is reflectivity and the vertical axis (z) is depth. The gray area represents noise, signals that exceed this threshold are considered to be reliable (with a confidence level of 95%). The stack for Path C uses 34 seismograms from 8 events.

Table 1. Source-receiver pairs used for path A - Marianas to Hawaii.

Event Date	Event Time (HH:MM:SS)	Latitude (Deg.)	Longitude (Deg.)	Depth (km)	Magnitude (Mw)	Stations Used
February 5, 2005	03:34:26	16.011	145.867	142.7	6.6	KIP
February 2, 2005	02:30:26	14.080	144.715	158.7	6.3	KIP
June 3, 2002	09:15:01	27.564	139.780	488.7	5.9	KIP
October 27, 2000	04:21:52	26.266	140.460	388.0	6.3	KIP
August 6, 2000	07:27:13	28.856	139.556	394.8	7.4	KIP
June 21, 2000	16:25:06	14.112	144.962	112.2	5.9	KIP
March 28, 2000	11:00:23	22.338	143.730	126.5	7.6	KIP, MAUI
February 15, 2000	02:05:01	17.675	145.401	521.5	5.9	KIP
July 3, 1999	05:30:10	26.323	140.482	430.6	6.1	KIP
January 12, 1999	02:32:26	26.741	140.170	440.6	6.0	KIP
September 8, 1998	09:10:03	13.257	144.007	141.0	6.1	KIP
May 15, 1998	05:58:06	14.178	144.880	154.0	6.1	KIP
April 23, 1997	19:44:28	13.986	144.901	101.0	6.5	KIP
July 15, 1996	16:51:22	18.726	145.628	177.0	6.3	KIP
July 6, 1996	21:36:29	21.968	142.830	241.0	6.2	KIP
February 14, 1996	21:26:56	29.246	140.446	141.3	6.0	KIP
October 20, 1995	19:21:29	18.708	145.544	224.8	6.1	KIP
August 24, 1995	07:54:43	18.823	145.042	612.4	6.2	KIP
August 24, 1995	06:28:55	18.847	145.123	602.2	6.2	KIP
August 23, 1995	07:06:03	18.856	145.218	594.9	7.1	KIP
April 8, 1995	17:45:13	21.833	142.691	267.4	6.7	KIP

Table 2. Source-receiver pairs used for path B - Japan to Hawaii.

Event Date	Event Time (HH:MM:SS)	Latitude (Deg.)	Longitude (Deg.)	Depth (km)	Magnitude (Mw)	Stations Used
November 12, 2003	08:26:46	33.631	137.020	391.1	6.4	KIP
July 27, 2003	06:25:32	47.151	139.248	470.3	6.8	KIP,MAUI
November 17, 2002	04:53:54	47.824	146.209	459.1	7.3	KIP
October 3, 2001	17:25:13	47.079	148.631	284.5	5.9	KIP
February 26, 2001	05:58:22	46.815	144.525	392.0	6.1	KIP
December 22, 2000	10:13:01	44.790	147.196	140.4	6.3	KIP,MAUI
July 10, 2000	09:58:19	46.828	145.422	359.6	6.1	KIP
May 12, 1999	17:59:22	43.032	143.835	102.7	6.5	KIP
November 15, 1997	07:05:17	43.813	145.019	161.0	6.1	KIP
December 22, 1996	14:53:28	43.207	138.920	227.0	6.5	KIP
February 22, 1996	14:59:09	45.263	148.542	124.2	6.3	KIP
February 1, 1996	07:18:04	44.853	146.273	170.0	6.2	KIP
March 31, 1995	14:01:41	38.150	135.058	365.0	6.2	KIP

Table 3. Source-receiver pairs used for path C - Sea of Japan to Honshu.

Event Date (MDDYYYY)	Event Time (HH:MM:SS)	Latitude (Deg.)	Longitude (Deg.)	Depth (km)	Magnitude (Mw)	Stations Used
August 31, 2003	23:08:01	43.476	132.238	479.6	6.2	MAJO
August 31, 2003	23:08:00	43.390	132.270	481.0	6.2	INU, ASI, FUJ, KNM, NAA, ONS, TGA, ADM, SBT, TTO
September 15, 2002	08:39:33	44.830	129.920	586.0	6.4	MAJO, INU, ASI, FUJ, HKW, KNM, NAA, ONS, SGN, TGA, YAS
June 28, 2002	17:19:30	43.752	130.666	566.0	7.3	MAJO, INU
June 28, 2002	17:19:30	43.750	130.670	566.0	7.3	INU, ASI, CHS, FUJ, GJM, HKW
February 13, 2000	02:57:09	42.853	131.572	513.6	6.0	MAJO
April 8, 1999	13:10:34	43.607	130.350	565.7	7.1	MAJO, TSK
April 8, 1999	13:10:34	43.610	130.350	565.0	7.1	TSK

Table 4. Station information.

Station Code	Station Name	Latitude (Deg)	Longitude (Deg)	Elevation (m)
ADM	Akadomari	37.905	138.430	276.0
ASI	Ashio	36.634	139.421	663.0
CHS	Choshi	35.706	140.852	52.0
FUJ	Fuji-kawa	35.231	138.472	140.0
GJM	Gojyoume	39.956	140.111	105.0
HKW	Honkawane	35.097	138.135	449.0
INU	Inuyama	35.349	137.017	140.0
KIP	Kipapa	21.423	-158.014	73.0
KNM	Kanayama	35.717	137.178	339.0
MAJO	Matsushiro	36.543	138.207	405.9
MAUI	Maui	20.768	-156.245	2060.0
NAA	Naalehu	19.063	-155.587	205.0
ONS	Onishi	36.156	138.982	477.0
SBT	Shibata	37.968	139.450	160.0
SGN	Turusugeno	35.510	138.944	800.0
TGA	Taga	35.185	136.338	290.0
TSK	Tsukuba	36.211	140.110	280.0
TTO	Takato	35.836	138.121	1150.0
YAS	Yuasa	34.033	135.182	10.0

Table 5. Crustal thickness, attenuation, depth, and reflectivity of modeled discontinuities.

Path	Crustal Thickness (km)	Attenuation (Qscs)	Discontinuity Depth (km)	Reflectivity (x100)
A	10	250	83 288 414 654	-5.22 +2.30 +3.35 +3.55
B	16	342	77 321 413 650 2645	-4.87 +1.46 +2.54 +5.03 +2.15
C	30	223	337 413 558 656 850 2782	-1.71 +4.01 +2.70 +6.00 +1.10 -9.40

CONTACT INFORMATION

Name:	Brian C. Bagley
Professional Address:	University of Minnesota 310 Pillsbury Drive SE Minneapolis, MN 55455-0219
Email Addresses:	bbagley@tamu.edu bagl0025@umn.edu
Education:	B. S., Geophysics, Texas A&M University, May 2006